

Tuning spin currents in collinear antiferromagnets and altermagnets

Sajjan Sheoran¹ and Pratibha Dev^{1, 2, *}

¹*Department of Physics and Astronomy, Howard University, Washington D.C., USA*

²*Laboratory for Physical Sciences, College Park, Maryland 20740, United States*

(Dated: December 4, 2025)

Spin current generation through non-relativistic spin splittings, found in uncompensated magnets and d -wave altermagnets, is desirable for low-power spintronics. Such spin currents, however, are symmetry forbidden in conventional collinear antiferromagnets and higher-order altermagnets. Using spin point group analysis, we demonstrate that finite spin currents can be induced in these materials via magnetoelectric, piezomagnetic, and piezomagnetoelectric-like couplings. We utilize electric fields, strain, and their combinations to drive symmetry-lowering phase transitions into uncompensated magnetic or d -wave altermagnetic states, thereby enabling finite spin conductivity in a broader class of magnetic materials. We further substantiate this framework using density functional theory and Boltzmann transport calculations on representative magnetic materials – KVSe_2O , RuF_4 , Cr_2O_3 , FeS_2 , and MnPSe_3 – spanning these different cases. The charge-to-spin conversion ratio reaches up to almost 100% via uncompensated magnetism and about 40% via d -wave altermagnetism under realistic conditions, highlighting the effectiveness of this approach for efficient spin current generation.

I. INTRODUCTION

The generation of pure spin currents is of fundamental interest in spintronics. In most materials, spin currents are typically achieved via the spin-Hall effect driven by spin-orbit interaction (SOI) [1, 2]. However, SOI, which gives rise to spin currents, also results in spin dephasing mechanisms, such as D'yakonov-Perel [3] and Elliott-Yafet processes [4, 5]. Such dephasing mechanisms limit the coherence length of the spin currents, thereby constraining their practical applications. Recently, collinear compensated magnets [6–9] and noncollinear antiferromagnets [10–12] have been shown to generate highly spin-polarized currents through exchange fields. The charge-to-spin conversion efficiency and coherence length of such nonrelativistic spin currents can exceed those of SOI-driven mechanisms by orders of magnitude [13–15].

In the context of symmetry, collinear compensated magnets are classified as antiferromagnets (AFMs) or altermagnets (AMs), depending on the symmetries that connect opposite spin sublattices [8]. In AFMs, the opposite spin sublattices are related by spatial inversion (P) and translation (τ), leading to spin-degeneracy and zero spin conductivity. In contrast, AMs have mirror-rotation symmetries connecting opposite spin sublattices, and are further categorized by their planar or bulk d -, g -, and i -wave orders. Spin current generation has been theoretically predicted in d -wave AMs, such as RuO_2 [13]. However, the altermagnetic ground state of RuO_2 is still under debate [15]. Unfortunately, spin conductivity remains forbidden in higher-order AMs (g - and i -wave) due to additional spin-degenerate nodal surfaces. Nevertheless, one can use strain and electric fields to manipulate the altermagnetic order to allow for spin currents [16–18].

For instance, recent works used uniaxial strain to induce g - to d -wave altermagnetic phase transitions in MnTe [16] and CrSb [17]. Other researchers showed that an electric field applied to the antiferromagnetic MnPSe_3 can induce a transition to either a d -wave [19] or an i -wave AM phase [20]. While most such studies have focused on altermagnetic spin splittings, a general framework for generating nonrelativistic spin currents via magnetic phase transitions has remained unexplored.

In this article, we provide a general approach based on spin group symmetry formalism to induce spin currents through magnetoelectric, piezomagnetic, and piezomagnetoelectric-like coupling. We show that electric (\mathcal{E}_i) and strain (η_{ij}) fields and their combination ($\mathcal{E}_i\eta_{jk}$) can be utilized to induce spin-currents in AFMs and higher-order AMs via reduction of their respective symmetries. By considering the lower effective spin point groups (SPGs) under external stimuli for all possible AFMs and higher-order AMs, we determine the correlation between spin current and \mathcal{E}_i , η_{jk} , and $\mathcal{E}_i\eta_{jk}$. We compute the spin-polarized conductivity for several representative examples of collinear compensated magnets using DFT and Boltzmann transport simulations. We also determine the spin conductivity for the reduced SPGs when the materials are subjected to an external electric field along an arbitrary direction.

II. COMPUTATIONAL DETAILS

In the nonrelativistic case, conductivity can be described through the spin-up (s_k) and spin-down ($-s_k$) channels with spin polarization along the k direction. Spin-polarized conductivity, $\sigma_{ij}^{s_k}$, is defined as $J_i^{s_k} = \sigma_{ij}^{s_k} \mathcal{E}_j$, where \mathcal{E}_j is the electric field along the j -direction and $J_i^{s_k}$ is the current along the i -direction. Within the Boltzmann transport theory, the conductivity $\sigma_{ij}^{s_k}$ (con-

* pdev@lps.umd.edu

tributed by $E_{n\mathbf{k}}$) is expressed as [21]

$$\sigma_{ij}^{s_k}(E_F) = -\frac{e^2\tau}{8\pi^3\hbar^2} \sum_n \int \frac{\partial E_{n\mathbf{k}}^{s_k}}{\partial k_i} \frac{\partial E_{n\mathbf{k}}^{s_k}}{\partial k_j} \frac{\partial f^0}{\partial E_{n\mathbf{k}}^{s_k}} d^3k \quad (1)$$

Here, τ is the relaxation time, and f^0 is the Fermi-Dirac distribution function. Within Eq. 1, the net charge and spin conductivity, respectively, are defined as

$$\begin{aligned} \sigma_{ij} &= \sum_k \sigma_{ij}^{s_k} + \sigma_{ij}^{-s_k} \\ \sigma_{ij}^k &= \frac{\hbar}{2e} (\sigma_{ij}^{s_k} - \sigma_{ij}^{-s_k}). \end{aligned} \quad (2)$$

The spin-polarized conductivity $\sigma_{ij}^{s_k}$ transforms under time-reversal (\mathcal{T}) as $\mathcal{T}\sigma_{ij}^{s_k} \rightarrow \sigma_{ij}^{-s_k}$. Accordingly, the charge and spin conductivity tensors are even and odd under time-reversal symmetry (\mathcal{T}), respectively. We initialize the spin-quantization axis along the z -direction. Since the effect of SOI is expected to be negligible, it is excluded from the simulation [13]. The absence of SOI means there is no spin canting, and consequently, $\sigma_{ij}^{x/y} = 0$. This can also be seen from Equation 1: $\sigma_{ij}^{s_k}$ transforms as $s_k k_i k_j$. The spin-only symmetry $[C_z(\pi) \parallel E]$ transforms $\sigma_{ij}^{s_x/s_y}$ to $\sigma_{ij}^{-s_x/-s_y}$, which implies that the net spin current, $\sigma_{ij}^{x/y}$, must vanish while the charge current can be nonzero. Therefore, under nonrelativistic collinear magnetism, the only allowed nonzero spin conductivity components are σ_{ij}^z . The shape of σ_{ij}^z is further restricted by the nontrivial spin group symmetry.

Density functional theory calculations were performed using the plane-wave ultrasoft pseudopotential [22] approach implemented in Quantum ESPRESSO [23]. The generalized gradient approximation with Hubbard correction (PBE+U) was used to treat exchange correlations self consistently [24]. The Kubo formalism, combined with DFT, was used to determine the charge and spin conductivities. To do so, we constructed a tight-binding Hamiltonian in the atom-centered Wannier basis [25] using the Wannier90 code [26]. In the single-particle energy eigenstate representation, the spin conductivity within the Kubo formalism is given by:

$$\begin{aligned} \sigma_{ij}^k &= -\frac{e\hbar}{2\Gamma} V \int \frac{d^3\mathbf{k}}{(2\pi)^3} \sum_n \langle n\mathbf{k} | \hat{J}_i^k | n\mathbf{k} \rangle \langle n\mathbf{k} | \hat{v}_j | n\mathbf{k} \rangle \\ &\quad \times \delta(E_{n\mathbf{k}} - E_F) \end{aligned} \quad (3)$$

where the $\hat{J}_i^k = \frac{1}{2} \{ \hat{v}_i, \hat{s}_k \}$ is the spin current operator. $\Gamma = \frac{\hbar}{2\tau}$ is a constant scattering rate, and is inversely proportional to the relaxation time, τ . The replacement of \hat{J}_i^k with \hat{v}_i^k in Eq. 3 gives the charge conductivity. The conductivity tensors were obtained by solving Eq. 3 as a postprocessing step of DFT calculations on a dense 350^3 k -mesh for 3D materials and 350^2 k -mesh for 2D materials, using the Wannier-Linear-Response code [13]. We made use of the Findsym [27], Bilbao Crystallographic Server [28], Findspingroup [29], and Tensor Sym-

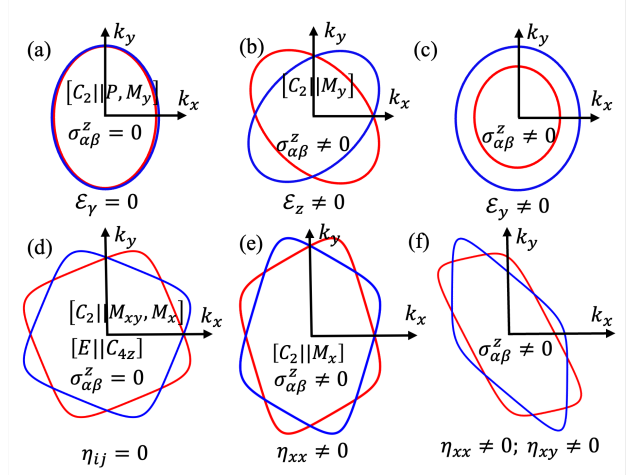


FIG. 1. Schematic of electric field and strain-induced spin conductivity. (a) Spin-polarized Fermi surface of an anti-ferromagnet with $[C_2 \parallel P]$ symmetry. The red and blue isosurfaces correspond to the opposite spin directions. Fermi surfaces of an antiferromagnet under an applied electric field when: (b) the effective spin group of the material possesses a symmetry connecting opposite spin sublattices (e.g., d -wave altermagnet with $[C_2 \parallel M_y]$), and (c) no such symmetry exists (ferromagnetic or compensated ferrimagnetic). (d) Fermi surface of a higher-order planar g -wave state. Fermi surfaces of a higher-order g -wave altermagnet (d) without strain and under a strain field η_{ij} when: (e) the effective spin group retains a symmetry connecting opposite spin sublattices (e.g., d -altermagnet with $[C_2 \parallel M_{xy}]$), and (f) no such symmetry remains. In the plots, Fermi surfaces are obtained from the minimal two-band models derived in Ref. [31], with strain effects incorporated using $k_i \rightarrow (\delta_{ij} + \eta_{ij})k_j$.

metry [30] packages to obtain the nontrivial SPGs and the corresponding shape of σ_{ij}^z .

III. SYMMETRY ANALYSIS

Collinear magnets are more accurately described using spin group symmetry operations of the form $[R_1 \parallel R_2]$, where R_1 and R_2 act on spin and real space, respectively [32]. These systems exhibit symmetries that fall into 32 SPGs associated with FM order, 22 SPGs corresponding to conventional AFM order, and 36 SPGs belong to AM order [29]. The spin group operations transform σ^{s_k} as

$$\mathbf{D}(R_2) \sigma^{\mathbf{D}(R_1)s_k} \mathbf{D}(R_2)^\dagger = \sigma^{s_k} \quad (4)$$

The spin conductivity component, σ_{ij}^z , will be allowed if the SPG does not contain any symmetry operation enforcing $\sigma_{ij}^{s_z} = \sigma_{ij}^{-s_z}$. Since the $[C_2 \parallel P]$ symmetry in AFMs leads to $\sigma^{s_k} = \sigma^{-s_k}$, the spin current σ^k is forbidden for all AFM SPGs, as schematically shown in Fig. 1(a) for SPGs containing $[C_2 \parallel P]$ and $[C_2 \parallel M_y]$. The $[C_2 \parallel P]$ symmetry can be broken by applying an electric field

TABLE I. Electric field-induced transition of antiferromagnetic SPG to ferromagnetic (or uncompensated magnetic) and altermagnetic SPG. The first column denotes the parent SPG, and the second, third, and fourth columns denote the effective SPG under the application of electric field \mathcal{E}_x , \mathcal{E}_y , and \mathcal{E}_z , respectively. The superscripts 1 and 2 preceding each symmetry operation indicate whether the spin sublattices are connected to the same or opposite spin sublattices. The SPG without any symmetry connecting opposite spin sublattices (SPGs with only superscript 1) are ferromagnetic. For the altermagnetic SPGs, the spin-orders (d , g , and i) are also indicated in parentheses.

SPGs	\mathcal{E}_x	\mathcal{E}_y	\mathcal{E}_z
$^2\bar{1}$	11	11	11
$^22/1m$	1m	$^22(d)$	1m
$^12/2m$	$^2m(d)$	12	$^2m(d)$
$^1m^2m^1m$	$^{22}2m^1m(d)$	$^{1m}1^{21}m(d)$	$^{1m}2m^22(d)$
$^1m^1m^2m$	$^{22}1m^2m(d)$	$^{1m}2^{22}m(d)$	$^{1m}1m^12(d)$
$^2m^2m^2m$	$^{12}2m^2m(d)$	$^{2m}1^{22}m(d)$	$^{2m}2m^12(d)$
$^14/2m$	$^2m(d)$	$^2m(d)$	14
$^24/2m$	$^2m(d)$	$^2m(d)$	$^{24}(d)$
$^{14}/2m^1m^1m$	$^{22}1m^2m(d)$	$^{1m}2^{22}m(d)$	$^{14}1m^1m$
$^{24}/2m^1m^2m$	$^{22}1m^2m(d)$	$^{1m}2^{22}m(d)$	$^{24}1m^2m(d)$
$^{14}/2m^2m^2m$	$^{12}2m^2m(d)$	$^{2m}1^{22}m(d)$	$^{14}2m^2m(g)$
$^2\bar{3}$	11	11	13
$^23^11^1m$	1m	$^22(d)$	$^{13}1^11m$
$^23^11^2m$	$^2m(d)$	12	$^{13}1^12m(g)$
$^26/1m$	1m	1m	$^{26}(g)$
$^16/2m$	$^2m(d)$	$^2m(d)$	16
$^{16}/2m^1m^1m$	$^{22}1m^2m(d)$	$^{1m}2^{22}m(d)$	$^{16}1m^1m$
$^{26}/1m^1m^2m$	$^{22}2m^1m(d)$	$^{1m}1^{21}m$	$^{26}1m^2m(g)$
$^{16}/2m^2m^2m$	$^{12}2m^2m(d)$	$^{2m}1^{22}m(d)$	$^{16}2m^2m(i)$
$^2m^2\bar{3}$	$^{12}2m^2m(d)$	$^{2m}1^{22}m(d)$	$^{2m}2m^12(d)$
$^2m^2\bar{3}^1m$	$^{24}2m^1m(d)$	$^{24}2m^1m(d)$	$^{24}2m^1m(d)$
$^2m^2\bar{3}^2m$	$^{14}2m^2m(g)$	$^{14}2m^2m(g)$	$^{14}2m^2m(g)$

(\mathcal{E}_i) since $[C_2||P]\mathcal{E}_i \rightarrow -\mathcal{E}_i$. The applied electric field (\mathcal{E}_i) also breaks the $[E||C_2||M_i]$ and $[E||C_2||C_{nj}(j \neq i)]$ symmetries. Overall, the spin conductivity component, σ_{ij}^z , becomes allowed if the electric field breaks all spin group symmetries that enforce $\sigma_{ij}^{sz} = \sigma_{ij}^{-sz}$. Table I lists the electric field-induced transitions of antiferromagnetic SPGs to either FM or AM SPGs. If the reduced effective SPG is an FM or a d -wave AM, a net spin current becomes allowed. In such a case, spin-polarized conductivity can be considered to be bilinear in the electric field. This coupling between spin current and electric field is reminiscent of magnetoelectric coupling. For instance, AFM SPG $^{12}/2m$ (two-fold axis along y -direction) reduces to the effective AM SPG of 2m under an electric field either applied along \mathcal{E}_x or \mathcal{E}_z . This case corresponds to the spin-polarized Fermi surface shown schematically in Fig. 1(b). Also, AFM SPG $^{12}/2m$ reduces to an effective FM SPG of 12 under electric field \mathcal{E}_y [spin-polarized Fermi surfaces in Fig. 1(c)]. Table I also lists the cases where the applied electric field reduces the AFM SPG to that of either a g - or an i -wave AM. For exam-

ple, \mathcal{E}_z applied to a $^{14}/2m^2m^2m$ or $^26/1m$ AFM, and \mathcal{E}_i ($i = x, y, z$) applied to a $^2m^2\bar{3}^2m$ AFM results in g -wave AMs. Also, the $^{16}/2m^2m^2m$ AFM reduces to an i -wave AM under the application of E_z . In such cases, a higher order (i.e., trilinear) electric field may be required to induce a finite spin conductivity [33].

Unlike the electric field that breaks the $[C_2||P]$ symmetry of AFMs, the strain field (η_{ij} , with $i, j = x, y, z$), which transforms like k_{ikj} , remains invariant under $[C_2||P]\eta_{ij} \rightarrow \eta_{ij}$. Therefore, η_{ij} is not sufficient to induce spin currents in AFMs. However, strain can be used to induce phase transitions in g - and i -wave AMs to obtain either an FM or a d -wave AM. For example, AM SPG $^{14}2m^2m$ is a g -wave altermagnet [see Fig. 1(d)]. The $[E||C_{4z}]$, $[E||M_x]$, and $[E||M_{xy}]$ symmetries would forbid a spin current in such a material. However, the application of the shear strain η_{xy} breaks $[C_2||M_x]$, leading to effective SPG $^2m^2m^12$ with spin-polarized Fermi surface similar to a d -wave AM as shown in Fig. 1(e). In addition, a simultaneous application of η_{xx} or η_{yy} along with η_{xy} , may break $[C_2||M_{xy}]$ as well, leading to an effective ferromagnetic SPG that has no symmetry connecting opposite spin sublattices. Therefore, in this case, the spin polarized Fermi surface is similar to that for an FM, as shown in Fig. 1(f). Table II lists the effective SPGs of g - and i -wave AMs under linear strain (η_{ij}) by collecting spin group symmetry operations $[R_1||R_2]$ such that $R_2\eta_{ij} \rightarrow \eta_{ij}$.

Our symmetry analysis shows how external stimuli, which break spin group symmetries that enforce zero spin conductivity, can be used to allow spin conductivity in a larger group of materials. It should be further noted that the symmetry-lowering stimuli in Tables I and Table II can be applied simultaneously to obtain spin conductivities in conventional magnets through piezomagnetoelectric-like ($\mathcal{E}_i\eta_{jk}$) couplings, where electric and strain fields act in concert. For example, AFM SPG $^{14}/2m^2m^2m$ allows spin conductivity under the application of $\mathcal{E}_z\eta_{ij}$, but not when \mathcal{E}_z or η_{ij} are used separately.

IV. DFT ANALYSIS

In this section, we use DFT-based calculations to investigate spin current generation in selected materials that are representative of the distinct symmetry cases summarized in Tables I and II. We begin by analyzing the spin conductivity in both bulk and two-dimensional d -wave AMs, which intrinsically support finite spin currents. Subsequently, we consider prototypical materials to explore three key mechanisms for spin current generation: (i) an electric field-driven transition from antiferromagnetic (AFM) to uncompensated magnetic order, (ii) a strain-induced symmetry transition from g -wave to d -wave AM, and (iii) a combined electric field and strain-mediated transition from i -wave to d -wave altermagnetism. Note that in accordance to Neumann's prin-

TABLE II. Tuning altermagnetism by the application of strain. The first and second columns denote the altermagnetic pattern and the parent SPG, respectively. The latter six columns denote the effective SPG of the parent space group after the application of the strain field η_{ij} .

Altermagnetic Pattern	SPGs	η_{xx}	η_{yy}	η_{zz}	η_{xy}	η_{xz}	η_{yz}
Planar g -wave	$^14/1 m^2 m^2 m$	$^2m^2 m^1 m$ (d)	$^2m^2 m^1 m$ (d)	$^14/1 m^2 m^2 m$ (g)	$^2m^2 m^1 m$ (d)	$^22/2 m$ (d)	$^22/2 m$ (d)
Planar g -wave	$^14^2 m^2 m$	$^2m^2 m^1 2$ (d)	$^2m^2 m^1 2$ (d)	$^14^2 m^2 m$ (g)	$^2m^2 m^1 2$ (d)	2m (d)	2m (d)
Planar g -wave	$^14^2 2^2 2$	$^22^2 2^1 2$ (d)	$^22^2 2^1 2$ (d)	$^14^2 2^2 2$ (g)	$^22^2 2^1 2$ (d)	22 (d)	22 (d)
Planar g -wave	$^1\bar{4}^2 2^2 m$	$^22^2 2^1 2$ (d)	$^22^2 2^1 2$ (d)	$^1\bar{4}^2 2^2 m$ (g)	$^2m^2 m^1 2$ (d)	22 (d)	22 (d)
Bulk g -wave	$^1\bar{3}^2 m^1 1$	$^22/2 m$ (d)	$^22/2 m$ (d)	$^1\bar{3}^2 m^1 1$ (g)	$^1\bar{1}$	$^1\bar{1}$	$^22/2 m$ (d)
Bulk g -wave	$^13^2 m^1 1$	2m (d)	2m (d)	$^13^2 m^1 1$ (g)	11	11	2m (d)
Bulk g -wave	$^13^2 2^1 1$	22 (d)	22 (d)	$^13^2 2^1 1$ (g)	11	11	22 (d)
Bulk g -wave	$^26/2 m$	$^22/2 m$ (d)	$^22/2 m$ (d)	$^26/2 m$ (g)	$^22/2 m$ (d)	$^1\bar{1}$	$^1\bar{1}$
Bulk g -wave	$^2\bar{6}$	2m (d)	2m (d)	$^2\bar{6}$ (g)	2m (d)	11	11
Bulk g -wave	26	22 (d)	22 (d)	26 (g)	22 (d)	11	11
Bulk g -wave	$^26/2 m^2 m^1 m$	$^2m^1 m^2 m$ (d)	$^2m^1 m^2 m$ (d)	$^26/2 m^2 m^1 m$ (g)	$^22/2 m$ (d)	$^12/1 m$	$^22/2 m$ (d)
Bulk g -wave	$^26^2 m^1 m$	$^2m^1 m^2 2$ (d)	$^2m^1 m^2 2$ (d)	$^26^2 m^1 m$ (g)	22 (d)	1m	2m (d)
Bulk g -wave	$^26^2 2^1 2$	$^22^1 2^2 2$ (d)	$^22^1 2^2 2$ (d)	$^26^2 2^1 2$ (g)	22 (d)	12	22 (d)
Bulk g -wave	$^2\bar{6}^2 m^1 2$	$^2m^1 2^2 m$ (d)	$^2m^1 2^2 m$ (d)	$^2\bar{6}^2 m^1 2$ (g)	2m (d)	12	2m (d)
Bulk g -wave	$^2\bar{6}^2 2^1 m$	$^22^1 m^2 m$ (d)	$^22^1 m^2 m$ (d)	$^2\bar{6}^2 2^1 m$ (g)	2m (d)	1m	22 (d)
Planar i -wave	$^16/1 m^2 m^2 m$	$^2m^2 m^1 m$ (d)	$^2m^2 m^1 m$ (d)	$^16/1 m^2 m^2 m$ (d)	$^12/1 m$	$^22/2 m$ (d)	$^22/2 m$ (d)
Planar i -wave	$^16^2 m^2 m$	$^2m^2 m^1 2$ (d)	$^2m^2 m^1 2$ (d)	$^16^2 m^2 m$ (i)	12	2m (d)	2m (d)
Planar i -wave	$^16^2 2^2 2$	$^22^2 2^1 2$ (d)	$^22^2 2^1 2$ (d)	$^16^2 2^2 2$ (i)	12	22 (d)	22 (d)
Planar i -wave	$^1\bar{6}^2 m^2 2$	$^2m^2 2^1 m$ (d)	$^2m^2 2^1 m$ (d)	$^1\bar{6}^2 m^2 2$ (i)	1m	22 (d)	2m (d)
Bulk i -wave	$^1m^1 \bar{3}^2 m$	$^{24/1} m^1 m^2 m$ (d)	$^{24/1} m^1 m^2 m$ (d)	$^{24/1} m^1 m^2 m$ (d)	$^2m^2 m^1 m$ (d)	$^2m^2 m^1 m$ (d)	$^2m^2 m^1 m$ (d)
Bulk i -wave	$^2\bar{4}^1 3^2 m$	$^{2\bar{4}^1} 2^2 m$ (d)	$^{2\bar{4}^1} 2^2 m$ (d)	$^{2\bar{4}^1} 2^2 m$ (d)	$^2m^2 m^1 2$ (d)	$^2m^2 m^1 2$ (d)	$^2m^2 m^1 2$ (d)
Bulk i -wave	$^24^1 3^2 2$	$^{24^1} 2^2 2$ (d)	$^{24^1} 2^2 2$ (d)	$^{24^1} 2^2 2$ (d)	$^{22^2} 2^1 2$ (d)	$^{22^2} 2^1 2$ (d)	$^{22^2} 2^1 2$ (d)

ciple, we only need to consider point group operations for the response tensors that represent macroscopic/bulk properties [34]. Hence, we have omitted the translation part from the symmetry operations. Also, we have omitted the spin-only symmetry group “ $\infty m 1$ ” from our discussion of SPGs as this continuous symmetry only enforces conditions on the transverse spin polarization response ($\sigma_{ij}^{x/y} = 0$), but imposes no conditions on σ_{ij}^z . Additionally, we define the charge-to-spin conversion ratio as $\frac{2e}{\hbar} \sigma_{ij}^z / \sigma_{ij}$ [16]. In the limiting case, when energy falls into a region without bands, the charge conductivity σ_{ij} approaches zero, and this ratio becomes mathematically indeterminate. To address this, we set the conversion ratio to zero whenever σ_{ij} falls below a defined threshold in the charge-to-spin conversion versus energy plots. Note that in semiconductors, hole or electron doping is required to observe spin transport. A low-level doping concentration ($\approx 2\%$) is sufficient to provide a stable carrier density while maintaining the compensated magnetic order [35].

A. d -wave AMs

KVSe₂O belongs to a broader class of materials crystallizing in the orthorhombic crystal structure with a space group of $P4/mmm$ [see Fig. 2(a)]. KVSe₂O is

a room temperature metallic altermagnet with quasi-one-dimensional Fermi sheets extending along the k_x and k_y direction, and quasi-2D Fermi pockets centered around the X and Y points as seen in Fig. 2(b). The SPG of KVSe₂O is $^24/1 m^1 m^2 m$, containing $[C_2||C_{4z}]$, $[E||P]$, $[E||M_z]$, $[E||M_x]$, and $[C_2||M_{xy}]$. Following Neumann’s principle, the symmetries of this material’s SPG are adopted by its spin anisotropy. Using the transformation rules of Eq. 1 and Eq. 2, $[C_2||C_{4z}]$ transforms $\sigma_{yy}^{sz} = \sigma_{xx}^{-sz}$, $\sigma_{xy}^{sz} = -\sigma_{yx}^{-sz}$, $\sigma_{zx}^{sz} = \sigma_{zy}^{-sz}$, and $\sigma_{zy}^{sz} = -\sigma_{zx}^{-sz}$. Therefore, $[C_2||C_{4z}]$ enforces $\sigma_{xz}^z = \sigma_{yz}^z = \sigma_{zx}^z = \sigma_{zy}^z = \sigma_{zz}^z = 0$. Furthermore, $[C_2||M_{xy}]$ transforms $\sigma_{xy}^{sz} \rightarrow \sigma_{yx}^{-sz}$, and hence, $\sigma_{xy}^z = \sigma_{xy}^{-z} = 0$ (Eq. 2). Following a similar procedure for all symmetry operations, the symmetry allowed components of the spin conductivity tensor are σ_{yy}^z and σ_{xx}^z , with $\sigma_{yy}^z = -\sigma_{xx}^z$. Figure 2(c) shows the spin conductivity, σ_{xx}^z , for the different scattering rates. The spin conductivity is inversely proportional to Γ within the considered range of 1 meV to 100 meV. The charge-to-spin conversion efficiency ($\frac{2e}{\hbar} \sigma_{ij}^k / \sigma_{ij}$) is 76%, which can reach almost 100% with electron doping of 0.5 eV [see Fig. 2(d)], where the Fermi pockets around the X and Y points vanish and spin currents are entirely governed by the Fermi sheets.

RuF₄ is a well known 2D d -wave AM crystallizing in space group $P2_1/c$ [see Fig. 3 (a)]. The SPG of RuF₄ is $^22/2 m$ with spin symmetry operations $[C_2||M_y]$ and

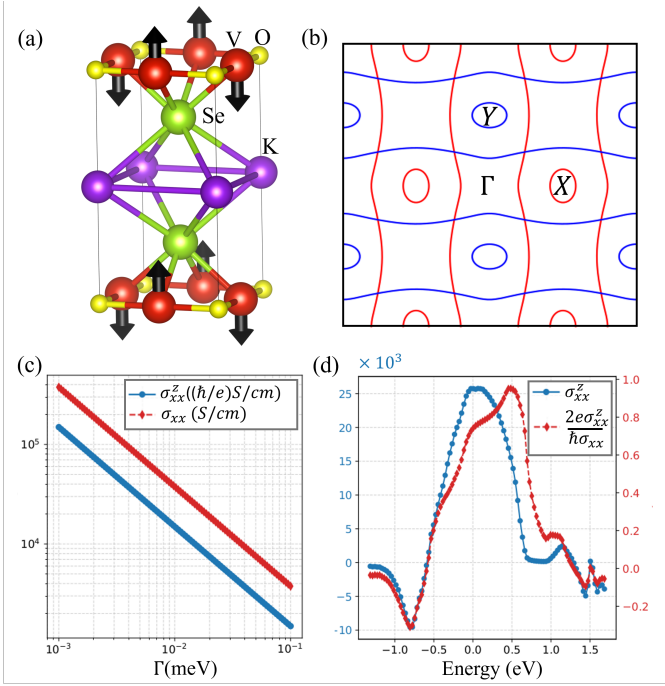


FIG. 2. (a) The crystal and magnetic structures of KVSe₂O. (b) The Fermi surface of KVSe₂O projected on the $k_z = 0$ plane, calculated without spin-orbit coupling. The red and blue curves denote spin-up and spin-down Fermi surfaces, respectively. (c) The charge and spin conductivity as a function of the scattering rate (Γ). (d) The spin conductivity and corresponding charge-to-spin conversion ratio as a function of the Fermi energy.

$[E||P]$ [see Fig. 3 (b)]. $[C_2||M_y]$ transforms $\sigma_{ii}^{sz} = \sigma_{ii}^{-sz}$, therefore $\sigma_{ii}^z = 0$. Also, $[C_2||M_y]$ leads to $\sigma_{xy}^{sz} = -\sigma_{xy}^{-sz}$, $\sigma_{yx}^{sz} = -\sigma_{yx}^{-sz}$, $\sigma_{xz}^{sz} = \sigma_{xz}^{-sz}$, $\sigma_{zx}^{sz} = -\sigma_{zx}^{-sz}$, $\sigma_{yz}^{sz} = -\sigma_{yz}^{-sz}$, and $\sigma_{zy}^{sz} = -\sigma_{zy}^{-sz}$. Therefore, the nonzero components of the spin conductivity tensor are σ_{xy}^z , σ_{yx}^z , σ_{yz}^z , and σ_{zy}^z . Since RuF₄ is a semiconductor, the charge conductivity is zero at the Fermi energy. Fig. 3(c) shows the spin conductivity, σ_{xy}^z , of the hole-doped RuF₄ as a function of the Fermi energy. The maximum charge-to-spin conversion efficiency is 80% when the hole doping moves the Fermi level below the intrinsic Fermi level by ~ 0.9 eV [Fig. 3(c)].

Note that although both KVSe₂O and RuF₄ are d -wave AMs, their respective responses to the applied electric field differ from each other. This is owing to the different spin anisotropies of their Fermi surfaces. In the case of RuF₄, the bands are spin-degenerate along the x and y directions, while for KVSe₂O, the bands are spin-degenerate along the $x + y$ and $x - y$ directions. Hence, if the applied electric field is in the x direction, KVSe₂O will show longitudinal spin conductivity while RuF₄ will exhibit transverse spin conductivity. On the other hand, KVSe₂O will exhibit transverse spin conductivity, and RuF₄ will show longitudinal spin conductivity when an electric field is applied along the $x + y$ or $x - y$ direction.

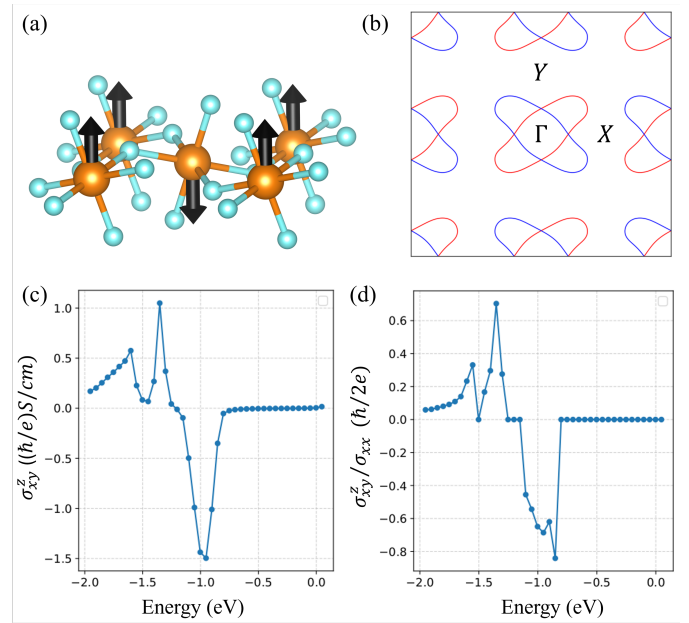


FIG. 3. (a) The crystal and magnetic structures of RuF₄. (b) The Fermi surface of RuF₄ projected on the $k_z = 0$ plane, calculated without spin-orbit coupling. (c) The spin conductivity and (d) corresponding charge-to-spin conversion ratio as a function of the Fermi energy.

The longitudinal and transverse spin conductivity for an arbitrary direction of the electric field for KVSe₂O and RuF₄ is plotted in Section I of the SM.

B. \mathcal{E}_z induced AFM to uncompensated magnetism

Bulk Cr₂O₃ is a well-known magnetoelectric antiferromagnet that crystallizes in the $\bar{R}\bar{3}c$ space group symmetry. The SPG of Cr₂O₃ is $\bar{2}\bar{3}11m$ with the following spin symmetry operations: $[C_2||P]$, $[E||M_y]$, $[E||C_{3z}]$, and $[C_2||S_{3z}]$ [see Fig. 4(a)]. Since the $[C_2||P]$ symmetry operation transforms σ_{ij}^{sz} to σ_{ij}^{-sz} , spin conductivity is forbidden in bulk Cr₂O₃. The application of \mathcal{E}_z breaks $[C_2||S_{3z}]$ and $[C_2||P]$, while preserving $[E||M_y]$ and $[E||C_{3z}]$ symmetries. This reduces the original SPG to a ferromagnetic $1\bar{3}11m$ SPG (see Table I). To apply the electric field, we used a [0001] film of Cr₂O₃ with a 20 Å vacuum separating the film from its image in the z -direction. This structure was previously found to result in the most stable surface [36]. Since the electric field, \mathcal{E}_z , breaks the $[C_2||P]$ symmetry, which is the only symmetry that connects the opposite spin sublattices, it leads to a Zeeman-like spin splitting of the conduction and valence bands, as seen in Fig. 4(b). Despite the presence of spin splitting, which is similar to that of a ferromagnet, our DFT calculations reveal a net zero magnetic moment. This apparent contradiction can be attributed to the semiconducting nature of Cr₂O₃, which gives rise to zero net magnetic moment according to the Luttinger's

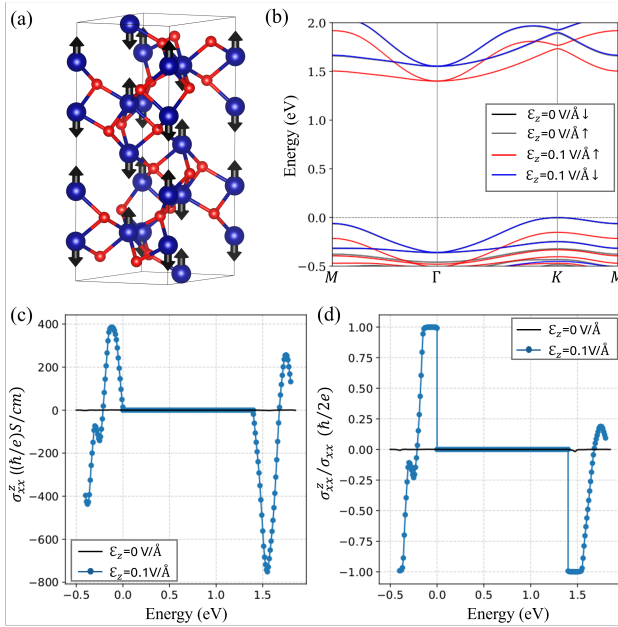


FIG. 4. (a) The crystal and magnetic structures of Cr_2O_3 . The blue and red spheres are used for Cr and O atoms, respectively. (b) Spin-polarized band structure of [0001] film of Cr_2O_3 with and without the electric field, ϵ_z . (c) The spin conductivity and (d) corresponding charge-to-spin conversion ratio as a function of the Fermi energy with and without ϵ_z .

criterion. In a stoichiometric compound, Luttinger's criterion requires that the net magnetization be equal to $N\mu_B$ ($N=\text{integer}$). When at least one spin channel is gapped (i.e. the material is either a semiconductor or a half metal), and the orbital moment is quenched, this results in zero net magnetic moment for small perturbations. The $[E||M_y]$ and $[E||C_{3z}]$ symmetries allow spin conductivity components – σ_{xx}^z , σ_{yy}^z , and σ_{zz}^z – to be non-zero, with $\sigma_{xx}^z = \sigma_{yy}^z$. It should be pointed out that since $J_x^z = \sigma_{xx}^z \mathcal{E}_x$ and σ_{xx}^z itself depends on \mathcal{E}_z , we get that $J_x \propto \mathcal{E}_x \mathcal{E}_z$. In other words, the spin conductivity is at least second order in the electric field. Figure 4(c) plots the spin conductivity, σ_{xx}^z , for the electron- and hole-doped Cr_2O_3 as a function of Fermi energy with and without an external electric field ($\mathcal{E}_z = 0.1 \text{ V}/\text{\AA}$). The spin conductivity σ_{xx}^z switches signs on going from negative values of Fermi energy (corresponding to hole-doping) to the positive values (electron doping). This is owing to the opposite spin magnetization of the topmost valence and lowest conduction bands. As seen in Fig. 4(c), the maximum value of σ_{xx}^z is $\sim 750(\hbar/e)S/\text{cm}$ for the electron-doped material. Fig. 4(d) plots the charge-to-spin conversion ratio as a function of Fermi energy. It is clearly seen that the charge current is fully spin polarized around the CBM and VBM, as only one type of spin-conduction channel contributes to the conductivity. On the other hand, away from the CBM and VBM, the charge-to-spin conversion ratio decreases as both spin conduction channels start contributing.

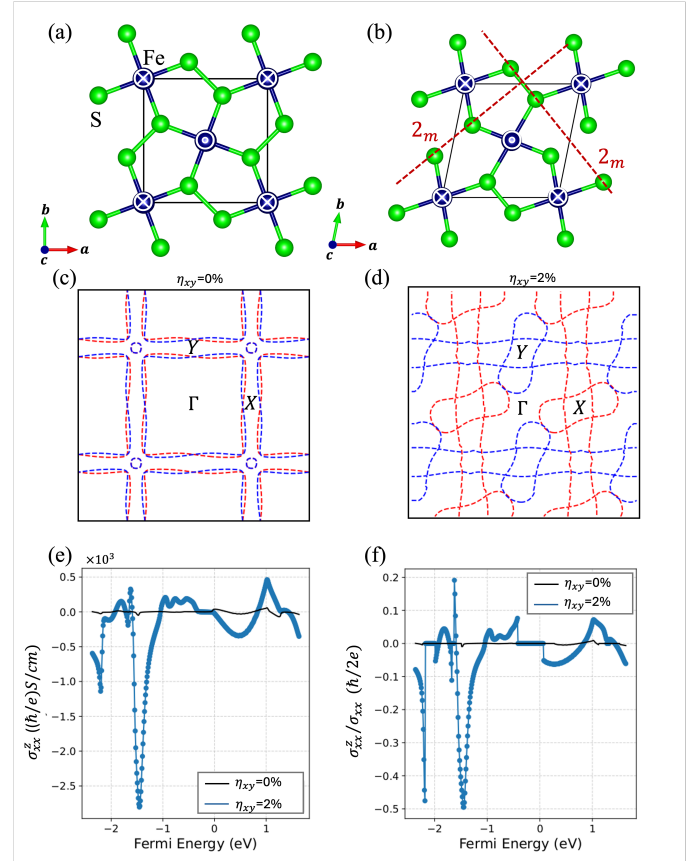


FIG. 5. (a) The crystal and magnetic structures of an FeS_2 monolayer (a) without and (b) with strain field, η_{xy} . The magnetic structures in (a) and (b) are shown by superimposing the \odot and \otimes symbols on the Fe atoms, representing spins that point in $+z$ (i.e out of the plane of paper) and $-z$ (into the plane of paper) directions, respectively. Also, in order to make the strain-induced distortions visible to the naked eye, we have exaggerated the strain to 20% in (b). The constant energy contours for (c) unstrained and (d) strained FeS_2 for $E_F = 1.45 \text{ eV}$ with maximum charge-to-spin conversion. The (e) spin conductivity and (f) charge-to-spin conversion ratio as a function of energy.

C. η_{xy} induced g -wave to d -wave transition

FeS_2 belongs to a large class of planar 2D materials that crystallize in the $P4/mbm$ space group [Fig. 5(a)]. FeS_2 is a planar g -wave AM with nontrivial SPG $1/4/1m^2m^2m$ containing $[C_2||M_x]$, $[C_2||M_{xy}]$, $[E||C_{4z}]$, and $[E||M_z]$. As discussed previously, the symmetry operation $[C_2||M_x]$ suppresses the following spin conductivity components: σ_{xx}^z , σ_{yy}^z , σ_{zz}^z , σ_{yz}^z , and σ_{zy}^z . Additionally, the mirror symmetry, $[E||M_z]$, eliminates σ_{xz}^z and σ_{zx}^z , while $[C_2||M_{xy}]$ forbids σ_{xy}^z and σ_{yx}^z . Therefore, spin current is completely forbidden in a planar g -wave AM. Consistent with the symmetry analysis, DFT calculations confirm a vanishing spin conductivity [see the solid black line in Fig. 5(e)]. The g -wave SPG $1/4/1m^2m^2m$ of FeS_2 reduces to a d -wave SPG $(2m^2m^1m)$ through applica-

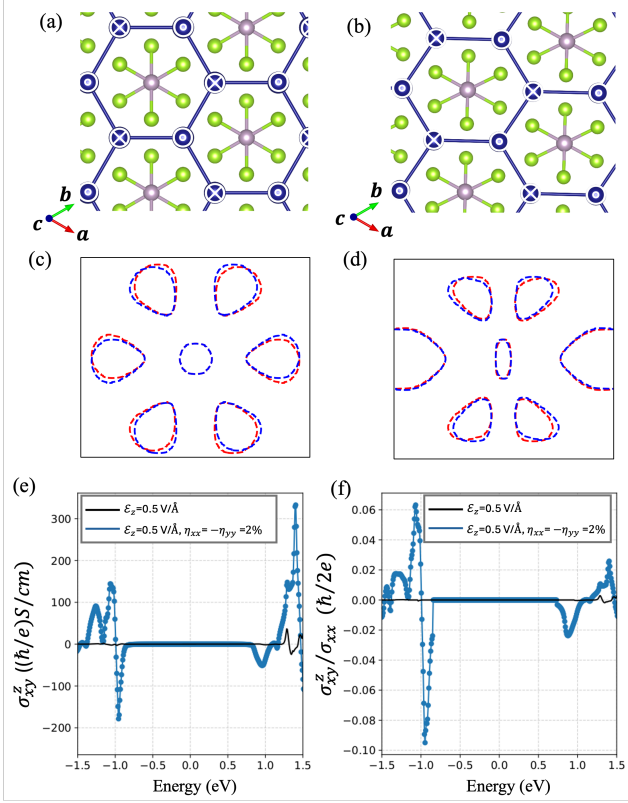


FIG. 6. (a) The crystal and magnetic structures of the monolayer MnPSe₃ (a) without and (b) with applied strain. In (b), the strain, $\eta_{xx} + \eta_{yy}$ (with $\eta_{xx} = -\eta_{yy}$), is exaggerated to 10% to magnify the structural distortions, making them visible to the naked eye. Also, the magnetization in (a) and (b) are shown by superimposing the \odot and \otimes symbols on the Mn atoms, representing spins that point in $+z$ (i.e. out of the plane of paper) and $-z$ (into the plane of paper) directions, respectively. The constant energy contours (at an energy of $E_F = 1.02$ eV) for (c) $\mathcal{E}_z = 0.5$ V/Å and (d) $\mathcal{E}_z = 0.5$ V/Å, and $\eta_{xx} = -\eta_{yy} = 0.02$, showing the *i* to *d* wave transition. The (e) spin conductivity and (f) charge-to-spin conversion ratio as a function of energy.

tion of η_{xx} , η_{yy} , or η_{xy} strains, whereas it can be reduced to a *d*-wave SPG ($^22/2^m$) through an application of η_{xz} or η_{yz} strains [see Table II]. As a representative case, we use the shear strain, η_{xy} , of 2%. The structural changes produced by this strain can be seen in Fig. 5 (b), where we have exaggerated the strain percentage to 20% for the sake of representation only. The SPG of FeS₂ under η_{xy} strain is $^2m^2m^1m$, with spin symmetry operations $[C_2||M_{xy}]$, $[C_2||M_{xy'}]$, and $[E||M_z]$. Therefore, $^2m^2m^1m$ allows for non-zero σ_{xx}^z and σ_{yy}^z components, with $\sigma_{yy}^z = -\sigma_{xx}^z$. Figures 5(c) and 5(d) show the antiferromagnetic phase transition from planar *g*-wave to planar *d*-wave upon the application of the strain. The maximum spin conductivity value is calculated to be up to $2800 \frac{\hbar}{e} \frac{S}{cm}$ as seen in 5(e). This occurs at an energy of -1.45 eV, where the Fermi surface is mostly composed of spin-polarized sheets along the *x* and *y* directions [Figs.

5(d) and 5(e)]. These Fermi sheets are similar to those for the case of KVSe₂O [Fig. 2(b)]. As seen in Fig. 5(f), the maximum spin-to-charge conversion ratio is 50%, which is smaller than that obtained for KVSe₂O due to the Fermi pockets around *X* and *Y*, which are slightly bigger than those of KVSe₂O [compare Figs. 2(b) and 5(d)]. Recall from subsection A that transverse spin conductivity will be observed when the electric field is applied along the $x \pm y$ directions [see section I of SM].

D. $\mathcal{E}_z \eta_{xx}$ induced AFM to *d*-wave AM transition

MnPSe₃ is a 2D antiferromagnet, which crystallizes in the $P31m$ space group [Fig. 6(a)]. The SPG of MnPSe₃ is $^2\bar{3}^2m^11$, and spin current is forbidden due to spin-degenerate bands. MnPSe₃ has been the subject of several reports that have studied its AFM to *d*-wave AM transition under the application of a vertical electric field [9, 37]. Under the application of an electric field (\mathcal{E}_z), the SPG of MnPSe₃ reduces from $^2\bar{3}^2m^11$ to $^13^2m^11$, with the latter containing $[E||C_{3z}]$ and $[C_2||M_x]$ symmetries [see Table I and Fig. 6(b)]. Although the $^13^11^2m$ SPG corresponds to the bulk *g*-wave AM, the 2D nature of MnPSe₃ ($k_z = 0$) makes it a planar *i*-wave AM [Fig. 6(c)]. The *i*-wave antiferromagnetic nature of monolayer MnPSe₃ can be confirmed from the six-fold symmetric constant energy-contours in Fig. 6(c). The spin currents are forbidden with and without the electric field due to underlying spin group symmetries $[E||C_{3z}]$ and $[C_2||M_x]$. This is due to the fact that $[E||C_{3z}]$ enforces $\sigma_{xx}^{sz} = \sigma_{yy}^{sz}$, $\sigma_{xy}^{sz} = -\sigma_{yx}^{sz}$, and $\sigma_{xz}^{sz} = \sigma_{yz}^{sz} = \sigma_{zx}^{sz} = \sigma_{zy}^{sz} = 0$, while the $[C_2||M_x]$ symmetry leads to $\sigma_{ii}^{sz} = \sigma_{ii}^{-sz}$, $\sigma_{yz}^{sz} = \sigma_{yz}^{-sz}$, $\sigma_{zy}^{sz} = \sigma_{zy}^{-sz}$, $\sigma_{xy}^{sz} = -\sigma_{xy}^{-sz}$, $\sigma_{yx}^{sz} = -\sigma_{yx}^{-sz}$, $\sigma_{xz}^{sz} = -\sigma_{xz}^{-sz}$, and $\sigma_{zx}^{sz} = -\sigma_{zx}^{-sz}$. However, the $^13^2m^11$ SPG can be further reduced to the 2m SPG by using η_{xx} , η_{yy} , and η_{yz} [Table II]. On the other hand, an application of either η_{xy} or η_{xz} reduces the SPG to that of an uncompensated magnet, while the $^13^2m^11$ SPG remains unaltered by the uniaxial strain along the *z*-direction (η_{zz}). Therefore, monolayer MnPSe₃ AFM will undergo a magnetic transition to a *d*-wave antiferromagnet under $\mathcal{E}_z \eta_{xx}$, $\mathcal{E}_z \eta_{yy}$, and $\mathcal{E}_z \eta_{yz}$. For illustrative purposes, we consider $\mathcal{E}_z(\eta_{xx} + \eta_{yy})$ with $\eta_{xx} = -\eta_{yy} = 0.02$, resulting in the structure shown in Fig. 6(b), and the corresponding constant energy contour in Fig. 6(d). The new SPG of MnPSe₃ under this strain is 2m , containing the $[C_2||M_x]$ symmetry operation [see Tables I and II]. As mentioned earlier, the only nonzero components of the spin conductivity tensor are σ_{xy}^z , σ_{yx}^z , σ_{yz}^z , and σ_{zy}^z . The σ_{yz}^z and σ_{zy}^z components are forbidden due to the 2D nature of MnPSe₃. Figures 6(e) and 6(f) show the spin conductivity and charge-to-spin conversion ratio for MnPSe₃ with electric field \mathcal{E}_z and $\mathcal{E}_z(\eta_{xx} + \eta_{yy})$. While there is no spin current in the absence of strain, the strain-induced charge-to-spin conversion ratio reaches up to $\sim 10\%$, which corresponds to a spin-splitter angle of approximately 11° . Here we have used the following expression for the spin-splitter

angle: $\theta_{ij} = \arctan\left(2 \frac{2e}{\hbar} \frac{\sigma_{ij}^s}{\sigma_{ii}^s}\right)$ [13, 17], with σ_{ij}^s (σ_{ij}^c) being the transverse spin conductivity (longitudinal charge conductivity). This spin-splitter angle is experimentally measurable [17, 38].

V. CONCLUSION

In this work, we have proposed a general framework to obtain nonrelativistic spin currents in collinear AFMs, and *g*- and *i*-wave AMs. Using symmetry analysis, we have demonstrated that spin conductivity can be induced through magnetoelectric, piezomagnetic, and piezomagnetoelectric-like couplings. The exact functional form of the spin-conductivity tensor is determined by the effective reduced SPG under the application of an external electric field and/or strain. By performing DFT calculations on realistic materials that were subjected to either electric fields, strains, or both, we have shown that the charge-to-spin conversion ratios in AFMs, as well as *g*- and *i*-wave AMs, can be as high as those seen for ferromagnets, compensated ferrimagnets, and *d*-wave altermagnets. It should be pointed out that the external stimuli considered in our work are realistic and can be achieved experimentally. For example, the direction-dependent strain field can be obtained by transferring the exfoliating altermagnetic crystals onto a flexible substrate with pre-patterned metal pads [39, 40]. The feasibility of our proposed approaches is also con-

firmed by recent reports of in-plane strain and magnetic field-induced nematicity in AFM intercalated transition metal dichalcogenides [41]. In addition, recently, finite anomalous Hall conductivity was successfully measured in the semiconducting *g*-wave AM, $\alpha\text{-Fe}_2\text{O}_3$, with 1% Ti doping [35]. Hence, doping to induce charge conductivity, along with electric fields and/or strain to drive the symmetry-lowering phase transitions, can be used to observe spin conductivity in intrinsically-semiconducting AFMs and higher-order AMs. Our proposed design principles for inducing spin currents are general and will expand the range of materials available for ultrafast magnetic spintronics.

ACKNOWLEDGMENTS

The research performed at Howard University was supported by Air Force Office of Scientific Research under award number FA9550-23-1-0679 and the National Science Foundation Grant No. DMR-1752840. This work used the Expanse cluster at SDSC through allocation PHY180014 from the Advanced Cyberinfrastructure Coordination Ecosystem: Services & Support (ACCESS) program, which is supported by National Science Foundation Grants Nos. 2138259, 2138286, 2138307, 2137603, and 2138296, and Maryland Advanced Research Computing Center.

[1] I. Žutić, J. Fabian, and S. D. Sarma, Spintronics: Fundamentals and applications, *Reviews of modern physics* **76**, 323 (2004).

[2] J. Hirsch, Spin hall effect, *Physical review letters* **83**, 1834 (1999).

[3] M. Dyakonov and V. Perel, Spin relaxation of conduction electrons in noncentrosymmetric semiconductors, *Soviet Physics Solid State, Ussr* **13**, 3023 (1972).

[4] R. J. Elliott, Theory of the effect of spin-orbit coupling on magnetic resonance in some semiconductors, *Physical Review* **96**, 266 (1954).

[5] Y. Yafet, Solid state physics. vol. 14/edited by f. seitz and d. turnbull (1963).

[6] S. Hayami, Y. Yanagi, and H. Kusunose, Bottom-up design of spin-split and reshaped electronic band structures in antiferromagnets without spin-orbit coupling: Procedure on the basis of augmented multipoles, *Physical Review B* **102**, 144441 (2020).

[7] L.-D. Yuan, Z. Wang, J.-W. Luo, and A. Zunger, Prediction of low-*z* collinear and noncollinear antiferromagnetic compounds having momentum-dependent spin splitting even without spin-orbit coupling, *Physical Review Materials* **5**, 014409 (2021).

[8] L. Šmejkal, J. Sinova, and T. Jungwirth, Beyond conventional ferromagnetism and antiferromagnetism: A phase with nonrelativistic spin and crystal rotation symmetry, *Physical Review X* **12**, 031042 (2022).

[9] S. Sheoran and P. Dev, Spontaneous anomalous hall effect in two-dimensional altermagnets, *Physical Review B* **111**, 184407 (2025).

[10] J. Železný, H. Gao, A. Manchon, F. Freimuth, Y. Mokrousov, J. Zemen, J. Mašek, J. Sinova, and T. Jungwirth, Spin-orbit torques in locally and globally noncentrosymmetric crystals: Antiferromagnets and ferromagnets, *Physical Review B* **95**, 014403 (2017).

[11] B. Flebus, Y. Tserkovnyak, and G. A. Fiete, Interfacial spin seebeck effect in noncollinear magnetic systems, *Physical Review B* **99**, 224410 (2019).

[12] S.-W. Cheong and F.-T. Huang, Altermagnetism with non-collinear spins, *npj Quantum Materials* **9**, 13 (2024).

[13] R. González-Hernández, L. Šmejkal, K. Výborný, Y. Yaghagi, J. Sinova, T. Jungwirth, and J. Železný, Efficient electrical spin splitter based on nonrelativistic collinear antiferromagnetism, *Physical Review Letters* **126**, 127701 (2021).

[14] H. Vakili, E. Schwartz, and A. A. Kovalev, Spin-transfer torque in altermagnets with magnetic textures, *Physical Review Letters* **134**, 176401 (2025).

[15] A. Bose, N. J. Schreiber, R. Jain, D.-F. Shao, H. P. Nair, J. Sun, X. S. Zhang, D. A. Muller, E. Y. Tsymbal, D. G. Schlom, *et al.*, Tilted spin current generated by the collinear antiferromagnet ruthenium dioxide, *Nature Electronics* **5**, 267 (2022).

[16] K. Belashchenko, Giant strain-induced spin splitting effect in mnte, ag-wave altermagnetic semiconductor, *Physical Review Letters* **134**, 086701 (2025).

[17] B. Karetta, X. H. Verbeek, R. Jaeschke-Ubiergo, L. Šmejkal, and J. Sinova, Strain controlled g-to d-wave transition in altermagnetic crsb, *arXiv preprint arXiv:2505.21293* (2025).

[18] L. Šmejkal, Altermagnetic multiferroics and altermagnetolectric effect, *arXiv preprint arXiv:2411.19928* (2024).

[19] D. Wang, H. Wang, L. Liu, J. Zhang, and H. Zhang, Electric-field-induced switchable two-dimensional altermagnets, *Nano Letters* **25**, 498 (2024).

[20] I. Mazin, R. González-Hernández, and L. Šmejkal, Induced monolayer altermagnetism in mnp (s, se) $_3$ and fese, *arXiv preprint arXiv:2309.02355* (2023).

[21] J. Callaway, *Quantum theory of the solid state* (Academic press, 2013).

[22] D. Vanderbilt, Soft self-consistent pseudopotentials in a generalized eigenvalue formalism, *Physical review B* **41**, 7892 (1990).

[23] P. Giannozzi, S. Baroni, N. Bonini, M. Calandra, R. Car, C. Cavazzoni, D. Ceresoli, G. L. Chiarotti, M. Cococcioni, I. Dabo, *et al.*, Quantum espresso: a modular and open-source software project for quantum simulations of materials, *Journal of physics: Condensed matter* **21**, 395502 (2009).

[24] J. P. Perdew, K. Burke, and M. Ernzerhof, Generalized gradient approximation made simple, *Physical review letters* **77**, 3865 (1996).

[25] N. Marzari and D. Vanderbilt, Maximally localized generalized wannier functions for composite energy bands, *Physical review B* **56**, 12847 (1997).

[26] A. A. Mostofi, J. R. Yates, Y.-S. Lee, I. Souza, D. Vanderbilt, and N. Marzari, wannier90: A tool for obtaining maximally-localised wannier functions, *Computer physics communications* **178**, 685 (2008).

[27] H. T. Stokes and D. M. Hatch, Findsym: program for identifying the space-group symmetry of a crystal, *Journal of Applied Crystallography* **38**, 237 (2005).

[28] M. I. Aroyo, J. M. Perez-Mato, C. Capillas, E. Kroumova, S. Ivantchev, G. Madariaga, A. Kirov, and H. Wondratschek, Bilbao crystallographic server: I. databases and crystallographic computing programs, *Zeitschrift für Kristallographie-Crystalline Materials* **221**, 15 (2006).

[29] X. Chen, J. Ren, Y. Zhu, Y. Yu, A. Zhang, P. Liu, J. Li, Y. Liu, C. Li, and Q. Liu, Enumeration and representation theory of spin space groups, *Physical Review X* **14**, 031038 (2024).

[30] R.-C. Xiao, Y. Jin, Z.-F. Zhang, Z.-H. Feng, D.-F. Shao, and M. Tian, Tensorsymmetry: a package to get symmetry-adapted tensors disentangling spin-orbit coupling effect and establishing analytical relationship with magnetic order, *arXiv preprint arXiv:2504.04424* (2025).

[31] M. Roig, A. Kreisel, Y. Yu, B. M. Andersen, and D. F. Agterberg, Minimal models for altermagnetism, *Physical Review B* **110**, 144412 (2024).

[32] D. B. Litvin and W. Opechowski, Spin groups, *Physica* **76**, 538 (1974).

[33] M. Ezawa, Third-order and fifth-order nonlinear spin-current generation in g-wave and i-wave altermagnets and perfectly nonreciprocal spin current in f-wave magnets, *Physical Review B* **111**, 125420 (2025).

[34] A. Cracknell, Symmetry properties of the transport coefficients of magnetic crystals, *Physical Review B* **7**, 2145 (1973).

[35] E. Galindez-Ruales, R. Gonzalez-Hernandez, C. Schmitt, S. Das, F. Fuhrmann, A. Ross, E. Golias, A. Akashdeep, L. Lünenbürger, E. Baek, *et al.*, Revealing the altermagnetism in hematite via xmcid imaging and anomalous hall electrical transport, *Advanced Materials* , e05019 (2025).

[36] A. L. Wysocki, S. Shi, and K. D. Belashchenko, Microscopic origin of the structural phase transitions at the cr 2 o 3 (0001) surface, *Physical Review B—Condensed Matter and Materials Physics* **86**, 165443 (2012).

[37] S. Sheoran and S. Bhattacharya, Nonrelativistic spin splittings and altermagnetism in twisted bilayers of centrosymmetric antiferromagnets, *Physical Review Materials* **8**, L051401 (2024).

[38] X. Tao, Q. Liu, B. Miao, R. Yu, Z. Feng, L. Sun, B. You, J. Du, K. Chen, S. Zhang, *et al.*, Self-consistent determination of spin hall angle and spin diffusion length in pt and pd: The role of the interface spin loss, *Science advances* **4**, eaat1670 (2018).

[39] J. Son, K.-H. Kim, Y. Ahn, H.-W. Lee, and J. Lee, Strain engineering of the berry curvature dipole and valley magnetization in monolayer mos 2, *Physical review letters* **123**, 036806 (2019).

[40] S. Sheoran, M. Jain, R. Moulik, and S. Bhattacharya, Probing the uniaxial strain-dependent valley drift and berry curvature in monolayer mosi 2 n 4, *Physical Review Materials* **7**, 114003 (2023).

[41] Z. Feng, W. Lu, T. Lu, F. Liu, J. R. Sheeran, M. Ye, J. Xia, T. Kurumaji, and L. Ye, Nonvolatile nematic order manipulated by strain and magnetic field in a layered antiferromagnet, *arXiv preprint arXiv:2507.05486* (2025).